applied optics

Interference of two diverging beams reflected from a plane parallel plate: stationary fringes with characteristic stable period

Hyesun A. Cha,[1,5] Byoung Joo Kim,[2] Myoungsik Cha,[1,2,*] Heejoo Choi,[3] and Dae Wook Kim[3,4]

[1]Institute for Extreme Physics, Pusan National University, Busan 46241, South Korea
[2]Department of Physics, Pusan National University, Busan 46241, South Korea
[3]Wyant College of Optical Sciences, University of Arizona, Tucson, Arizona 85721, USA
[4]Department of Astronomy & Steward Observatory, University of Arizona, Tucson, Arizona 85721, USA
[5]Current address: Department Electrical and Computer Engineering, Seoul National University, Seoul 08826, South Korea
*Corresponding author: mcha@pnu.edu

Received 18 June 2020; revised 30 August 2020; accepted 31 August 2020; posted 1 September 2020 (Doc. ID 399942); published 24 September 2020

We investigated interference fringes due to superposition of diverging light waves reflected from the two sides of a plane parallel plate. A non-localized fringe pattern of high contrast was obtained as a function of incident angle when we used a coherent diverging beam. We found that the fringe density increased to a certain angle and then decreased thereafter, against the common belief that the fringe density increases monotonically with the angle of incidence. Because the fringe density is maximum at this angle and does not change rapidly in the vicinity, we could employ Fourier analysis to estimate interferometric parameters, such as thickness, refractive index, and wavelength, that determine the characteristic stationary fringe density. © 2020 Optical Society of America

https://doi.org/10.1364/AO.399942

1. INTRODUCTION

Metrology using interferometers provides precise estimates of physical quantities and constants. Since its successful demonstration in astronomical measurements [1], interferometry has been developed as one of the most reliable metrological tools, and recently, the most sophisticated interferometers have been built to detect space distortions much smaller than the size of a proton, proving the existence of gravitational waves [2]. Although a variety of interferometers and interference effects have been studied and utilized for specific metrological applications, the main idea of such interferometric measurements lies in retrieving the phase information of light [3–8].

Here, we investigated the reflected interference fringes from transparent plane parallel plates (PPP), when illuminated with a coherent diverging light beam. The fringes are formed by the interference between mainly the two reflected diverging beams: one reflected from the first (upper) surface, and the other reflected internally from the second (bottom) surface, as described in Fig. 1. Although there are light waves emerging from the PPP after multiple internal reflections, they do not contribute significantly to the interference because they are much weaker than the first two reflected lights unless the refractive index of the PPP material is large or the angle of incidence approaches $\pi/2$. Therefore, for most glass plates with $n \sim 1.5$, non-localized fringes are formed practically by superposition of the two diverging waves from the image point sources, A_1 and A_2, as depicted in Fig. 1.

The first image point (A_1) is simply the mirror image of the point source A by the top surface. The position of the second image conjugate point (A_2) can also be determined by the mirror image of A by the bottom surface, including the refraction effect through the medium. If one assumes that the position of A_2 does not change with the angle of incidence, the constant-phase surfaces would be described by the hyperboloids whose surfaces pass between the two image points A_1 and A_2 [9]. Moreover, if the PPP is thick enough (~1000 wavelengths), one would expect a dense fringe pattern as a function of angle of incidence whose spacing decreases monotonically with increasing angle of incidence, approaching the case of the double-slit experiment.

However, we found that the fringe density increased to a certain angle, and then decreased as the angle of incidence further increased, against the common belief that the fringes would become denser for larger angles of incidence. This phenomenon is related to the fact that the location of the second image A_2 changes with the angle of incidence due to refraction. The existence of a *stable angle*, where the fringe density is maximum,

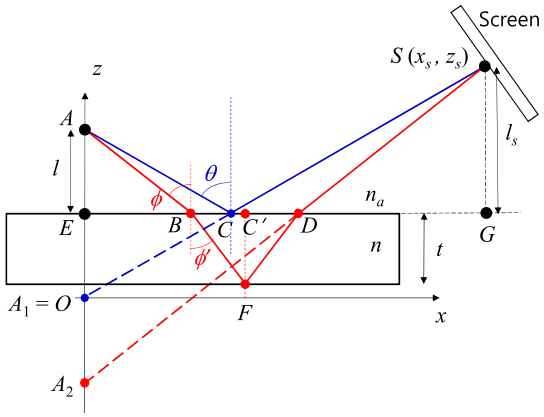

Fig. 1. Two rays emanating from a point source (A) are reflected from two sides of a plane parallel plate (PPP) and interferes at a point S on the screen. The thickness and the index of refraction of the PPP are t and n, respectively. A_1 is the image of A upon reflection at the top surface, while A_2 is the reflected image by the bottom surface. In Gaussian optics, A_2 lies on the z axis and $\overline{A_1A_2} = 2t/n$.

allows a standard Fourier analysis of the fringes around it, the principles of which we have demonstrated with a glass plate and an anisotropic crystal plate.

2. CALCULATION OF PHASE DIFFERENCE

Figure 1 shows a schematic diagram of our interference configuration using a transparent plate. The two (top and bottom) surfaces of the plate are assumed to be perfectly planar and parallel to each other, treating the plate as an ideal PPP. (A more general case of a wedged plate is discussed in Appendix B.) A spherical wave emanating from a coherent point source A is reflected by the two surfaces of the PPP, and then interferes on a screen. In the diagram, we show two rays that intersect at a specific point S on the screen. One can interpret that the interference fringes are formed by the superposition of the two spherical waves emanating from the two virtual point sources (A_1 and A_2), which are the mirror images of the real point source (A).

According to Gaussian optics, the second image is formed at a distance of $2t/n$ from the first image along the optical axis (z axis) due to the refraction inside the PPP with a thickness t. In this case, the fringe density would increase monotonically with the angle of incidence, negating the existence of a stable angle. However, it should be noted that the paraxial approximation cannot be used for large angles of incidence. This can be seen when looking obliquely at an object submerged in a medium (for example, water). In this case, the object appears closer to the surface than it would look when it is viewed from right above. The apparent depth of a point object can be calculated as

$$d' = \frac{d}{n}[1 - (n^2 - 1)\tan^2(\theta')]^{3/2}, \tag{1}$$

where d is the geometrical depth from the medium surface, n is the relative index, and θ' is the internal angle of incidence from the point object. (See Appendix A for derivation.) The image is also laterally shifted by

$$\Delta x = d(n^2 - 1)\tan^3\theta'. \tag{2}$$

When $\theta' = 0$ (normal incidence), we can confirm that $d' = d/n$ and $\Delta x = 0$. As the viewing angle increases, however, the image rapidly gets closer to the surface and the viewer. This phenomenon is the fundamental cause of the existence of a stable angle. It should be noted that Eqs. (1) and (2) were derived directly from the law of refraction without using any other approximations. Although adding a third-order correction term to the Gaussian optics can predict a similar result at small angles, it shows a large discrepancy for large angles ($\theta' \sim 1$).

By the same token, the second image for the PPP in Fig. 1 moves significantly with the angle of incidence. Therefore, we need to calculate the optical path length difference (OPD) between the two rays based on the laws of reflection and refraction without using any approximation. For convenience, we take our coordinate system as shown in Fig. 1, with the first image point A_1 as the origin. The optical path length of the first ray (blue line in Fig. 1) is

$$L_1 = n_a(\overline{AC} + \overline{CS}) = n_a\,\overline{OS} = n_a r, \tag{3}$$

where n_a is the refractive index of the atmosphere and $r = \overline{OS}$.

Meanwhile the optical path length of the second ray (solid red line in Fig. 1) is

$$L_2 = n_a(\overline{AB} + \overline{DS}) + n(\overline{BF} + \overline{FD}) = \frac{n_a(l + l_s)}{\cos\phi} + \frac{2nt}{\cos\phi'}$$
$$= \frac{n_a r\cos\theta}{\cos\phi} + \frac{2nt}{\cos\phi'}. \tag{4}$$

Here, t and n are the thickness and the refractive index of the PPP, respectively, l and l_s are the distances from the top surface of the PPP to the point source A and observation point S, respectively. ϕ' is the angle of refraction that is related to the angle of incidence ϕ by the law of refraction,

$$\sin\phi = n_r \sin\phi', \tag{5}$$

where $n_r = n/n_a$ is the relative refractive index of the PPP. The angles for the second ray can be determined by the relation

$$\overline{EG} = \overline{EB} + \overline{BD} + \overline{DG}. \tag{6}$$

As $\overline{EG} = r\sin\theta$, $\overline{EB} = l\tan\phi$, $\overline{DG} = l_s\tan\phi$, $\overline{BD} = 2t\tan\phi'$, and $l + l_s = y_s = r\cos\theta$, Eq. (6) becomes

$$r\sin\theta = r\cos\theta\tan\phi + 2t\tan\phi'. \tag{7}$$

Therefore, the angles of incidence and refraction of the second ray (ϕ and ϕ') are determined as functions of incident angle of the first ray θ by solving the coupled Eqs. (5) and (7). With these angles, the phase difference between the two rays can be obtained using Eqs. (3) and (4) as

$$\Phi(\theta) = \frac{2\pi}{\lambda}(\mathrm{OPD}) = \frac{2\pi}{\lambda}(L_2 - L_1)$$
$$= \frac{2\pi n_a r}{\lambda}\left(\frac{\cos\theta}{\cos\phi} - 1 + \frac{t}{r}\frac{2n_r}{\cos\phi'}\right). \tag{8}$$

3. NUMERICAL SIMULATION ON THE FRINGE DENSITY

The stationary fringe pattern can be numerically calculated using the phase difference in Eq. (8). Given ϕ and ϕ' by Eqs. (5) and (7), the phase difference can be expressed as a function of θ, with r, t, and n_r as parameters. Considering a phase delay of π due to the reflection at the top surface (i.e., reflection from a low-toward-high refractive index interface), destructive interference occurs at an angle satisfying $\Phi(\theta) = 2\pi m$, where m is an integer. Figure 2(a) shows the calculated $\Phi(\theta)$ for a 1 mm thick BK7 glass plate case. Because it ranges from 20,700 to 15,500 rad throughout the entire angle of incidence, one can expect ~100 fringes or more within a practical angular range of beam divergence.

We also note that the graph in Fig. 2(a) has an inflection point (i.e., characteristic stationary fringe condition), indicating that the fringe density, defined as

$$f(\theta) = \frac{1}{2\pi}\left|\frac{d\Phi(\theta)}{d\theta}\right|, \tag{9}$$

has an extremum as shown in Fig. 2(b). This cannot be expected within the Gaussian approximation giving fixed image points, where the fringe density is expected to increase monotonically.

For $r = 100$ mm and $n_r = 1.509$ at 915 nm for BK7 [10], the stable angle was calculated to be $\theta_s = 49.6°$. θ_s is smaller for a larger refractive index, but does not depend on the wavelength. The maximum fringe density (f_s) is almost proportional to the wave number ($\sim\lambda^{-1}$) as can be inferred from Eq. (8), with a small departure due to the dispersion of the PPP material. This property can be utilized to measure the wavelength of a light source [11]. We also note that the stable angle in Fig. 2(b) approaches that of the Haidinger fringes as the distance to the observation point becomes much larger than the thickness (t) of the PPP [11]. We have confirmed this limiting behavior for $r \gg t$ using numerical simulations. Therefore, the overall characteristics of the fringes can be conveniently predicted by the analytical expressions for the Haidinger fringes [11]. In the experiment, the fringe density was measured applying a fast Fourier transform (FFT) routine on the fringe data in a certain angular range around the calculated θ_s, finding the maximum fringe density f_s.

4. EXPERIMENTAL VERIFICATION

The experimental setup to verify and demonstrate the stationary fringe phenomenon was configured using a PPP and a light source. We used a fiber-coupled laser diode (Qphotonics, model QFBGLD-915-5) generating a single wavelength output at 915 nm with a linewidth of 1 MHz to produce a high-contrast interferometric fringe pattern. The single-mode fiber had a numerical aperture of 0.14, and the output beam from the exit end was linearly polarized. The naturally diverging beam from the fiber end was used as the light source in our experiment. The fiber end was placed ~10 mm apart from the top surface of a 1 mm thick BK7 glass plate, acting as a point source A in Fig. 1. We used a near-TE-polarization configuration to obtain a significant reflectance. Except the amount of reflection, the polarization had little effect on the fringe contrast, stable angle, and fringe density.

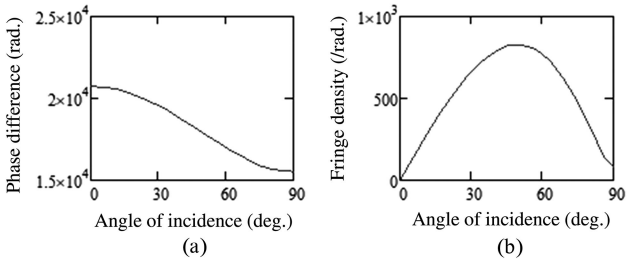

Fig. 2. (a) Phase difference between the two rays reflected from 1 mm thick BK7 glass plate in Fig. 1, and (b) the fringe density. Simulation parameters: $r = 100$ mm, $n_r = 1.509$, and $\lambda = 915$ nm.

The PPP was oriented approximately to an incident angle of $\theta_s = 49.6°$ relative to the axis of the diverging beam. Then, a linear CCD array (Alphalas, CCD-S3600-D) was placed 90 mm away from the plate to measure the interference fringes, aligning the CCD plane perpendicular to the reflected beam axis. The geometrical distance of the ray from the end of the fiber to the center of the CCD array via reflection from the top surface of the plate was ~100 mm. The CCD had a total of 3,600 pixels that could record the fringes in an angular range of about 16°.

Figure 3 shows a set of recorded CCD data for the interference fringes. The fringe contrast is close to 1, owing to the high coherence of the diode laser used in the experiment and negligible contributions from the multiple internal reflections. By analyzing the fringes with a FFT routine, a spectrum with a sharp peak was obtained, as shown in Fig. 4(a), which enabled us to read the fringe density at the corresponding pixel. To be specific, the fringe data in Fig. 3 were supplemented with sufficient zero-padding and multiplied by a Gaussian window with a width of 200 pixels before the FFT treatment. The fringe density in Fig. 4(b) was obtained by recording the location of the peak in the FFT spectrum while scanning the Gaussian window to obtain local fringe densities [11]. We used the FFT routine in MATLAB, installed on a personal computer. It shows a maximum around pixel number of 2,500 corresponding to ~50°, which roughly agrees with our numerical prediction in Fig. 2. Employment of the FFT was possible because the fringe density around the stable angle did not vary rapidly with angle.

In the preceding analysis, we assumed an ideal PPP where the two surfaces are perfectly parallel. However, commercially available glass plates and crystal wafers may have wedge angles of ~0.1 mrad. The BK7 glass plate used in our experiment had a smaller wedge angle because we did not observe Fizeau fringes on the surface of the plate (25 mm in diameter) upon viewing the reflection of a monochromatic lamp. We recalculated the phase difference $\Phi(\theta)$ for a plate with a wedge angle of α following the procedure described in Appendix B, numerically verifying that the stable angle and fringe density changed by only 1.8 μrad and 1.6 ppm, respectively, for a BK7 plate with $\alpha = 0.1$ mrad when $\beta \equiv l/(l + l_s) = 0.1$. It is a great advantage of this method that the analysis results are not very sensitive to the wedge angle of the plate.

The preceding Fourier analysis can be applied to the measurement of the wavelength of a light source or the refractive index of a semi-transparent material of which the PPP is made. When the thickness and refractive index of the PPP are known, the wavelength of the light source can be related to the maximum

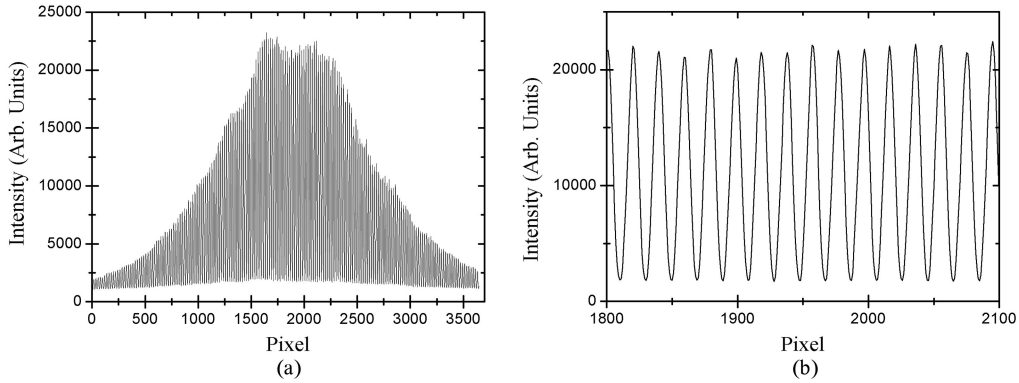

Fig. 3. (a) Raw fringe data from linear CCD array for 1 mm thick BK7 glass plate illuminated by 915 nm laser. (b) Expanded view of (a) between pixels 1800 and 2100. The center (∼pixel 1900) corresponds to an incident angle of 48°.

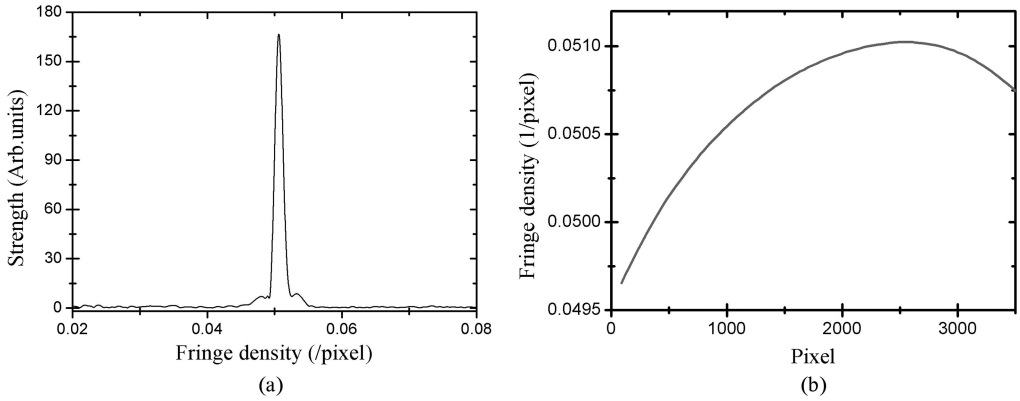

Fig. 4. (a) FFT spectrum of the fringe data in Fig. 3(a) near the stable angle. (b) Fringe density [peak in (a)] versus center location of the Gaussian window.

fringe density, enabling the wavelength measurement. This analytical model can be configured in various optical layouts and applied to measure interferometric parameters. We expect an uncertainty level of $\sim 5 \times 10^{-5}$ for the measurements as in [11], because their fringe characteristics and the analysis procedure are very similar to those of the current work.

5. STATIONARY FRINGES FOR A BIREFRINGENT CRYSTAL

When the wavelength of the light source is known, the refractive index can be estimated using the same method. As a demonstration, we measured the interference pattern reflected from a 1 mm thick x-cut congruent $LiNbO_3$ crystal (LN) plate. Congruent LN has a large birefringence; the refractive index is 2.243 for ordinary polarization, while it is 2.165 for extraordinary polarization for $\lambda = 915$ nm at 22°C [12]. The stable angles were calculated as 46.6° and 46.7° for the ordinary and extraordinary waves, respectively, where the maximum fringe densities were estimated to be 513.6/rad and 534.3/rad, respectively. The optic axis of the LN plate, parallel to the surfaces, was aligned parallel to the x axis defined in Fig. 1. Then, the 915 nm laser was linearly polarized at 45° with respect to the crystalline optic axis, and the angle of incidence was set to 47°.

The interference pattern reflected from the LN plate had smaller fringe density than that for the BK7 glass plate with a similar thickness, and exhibited a modulating envelope as shown in Fig. 5(a). This low-frequency modulation can be attributed to the beating of two fringes with different fringe densities caused by the different ordinary and extraordinary refractive indices. This is supported by the FFT spectrum in Fig. 5(b) showing two distinct peaks. We followed the same FFT procedure as in the fringe analysis of the BK7 PPP. Because the fringe density is sensitive to the refractive index, the index values can be easily estimated by reading the peaks of the FFT spectrum of the fringes. If we compare the maximum fringe density in Fig. 4 for BK7 with those in 5(b) for LN, the latter are significantly smaller than the former, because the indices of LN are much larger than that of BK7.

Here, we estimated the indices of LN based on the known index of BK7 (1.509 at 915 nm [10]) as follows: From Figs. 4(a) or 4(b), one can read the maximum fringe density as 510/pixel for the BK7 PPP, while it is estimated to be 828/rad in Fig. 2(b) using Eqs. (8) and (9), resulting in a calibration relation between the number of pixels and angular range in the stable region: 1 pixel $= 6.158 \times 10^{-5}$ rad. For the LN plate, the maximum fringe densities of 0.0316 and 0.0329/pixel are obtained from the two peaks in Fig. 5(b), which can be converted to 513 and 534/rad, respectively, using the calibration relation. From Eqs. (8) and (9), we found that these maximum fringe densities can be produced when the index values are 2.25 and 2.17, respectively, which agree with the ordinary and extraordinary

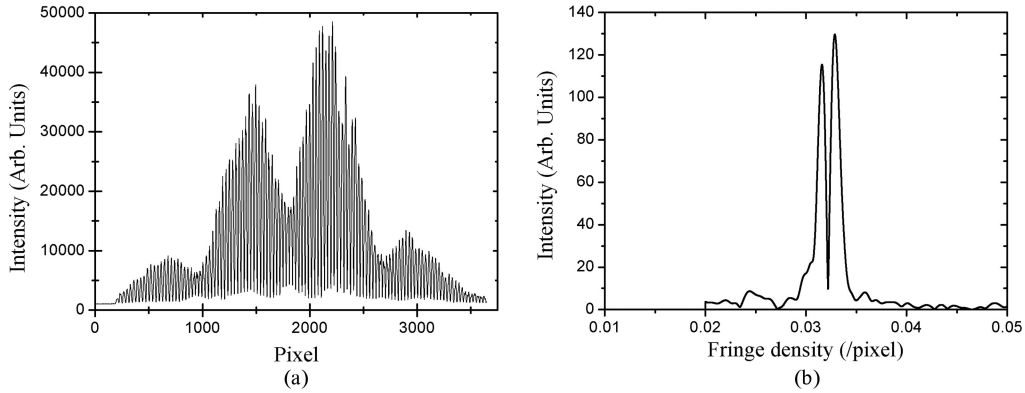

Fig. 5. (a) Stationary fringes from 1 mm thick birefringent LN plate, and (b) corresponding FFT spectrum (Gaussian window centered at pixel 1663). TE component was ordinary, while TM component was extraordinary.

indices obtained by the established Sellmeier equations for congruent LN [12]. If a more careful calibration is provided using a few more index references, we expect a much higher accuracy in the index measurements.

We acknowledge that the polarization-dependent analysis was not considered in the analysis of the fringes from the LN PPP. A rigorous analysis would require a full polarization analysis and non-sequential ray tracing as a function of incident angle using the configuration-specific birefringence of the crystal plate. A polarization-dependent stationary fringe analysis remains a good topic for future investigation.

Finally, we tested the possibility of a laser with poor coherence being used in the interference experiment. When the same experiment was repeated on the BK7 plate using a laser diode (wavelength of 635 nm) with a large linewidth (~0.5 nm), the fringe contrast was about 0.5, which was worse than the that of the fringes in Fig. 3. Such a poorer fringe contrast can be explained by the fact that the OPD between the two interfering lights was larger than the coherence length of ~0.8 mm, corresponding to a linewidth of 0.5 nm. When this laser was used for the LN plate, the fringe contrast of the reflected fringes was even worse, which can be attributed partly to the larger refractive index of LN (~2.2) than that of BK7 (~1.5). In the case of the LN plate, the light rays emerging after experiencing more than one internal reflection would have larger contributions to the interference than in the BK7 case because of the larger Fresnel reflections. In general, they make contributions that are out of phase with the fringes formed by the two major interfering rays, deteriorating the fringe contrast further. For a 1 mm thick BK7 plate, however, a light source with a medium coherence can also be used in the interferometry because the reflected fringes showed a reasonable contrast. A thicker PPP would produce fringes with larger density, facilitating the FFT analysis, but a light source with a higher coherence is required.

6. CONCLUSION

We investigated the nontrivial stationary interference fringes of diverging light waves reflected from the two sides of a PPP. Nonlocalized fringes with high contrast were obtained as a function of incident angle. The fringe density increased to a maximum and then decreased thereafter, against the common belief that the fringes would become denser for larger angles of incidence. This characteristic phenomenon allowed us to utilize a FFT routine for a simple but precise fringe analysis within the stable fringe density range. We expect that our method can be applied to a simple and robust apparatus for measuring the thickness of a PPP, source wavelength, or refractive index of the PPP material (isotropic or anisotropic).

APPENDIX A: IMAGE LOCATION OF AN OBJECT SUBMERGED IN OPTICALLY DENSE MEDIUM

Let us consider a point source A submerged in a medium with a higher index n_w, as shown in Fig. 6. We determine the coordinates of the image point A' using the law of refraction, without employing a paraxial approximation. Consider two rays $\overline{AP}$ and $\overline{AQ}$ that make angles of incidence of θ and $\theta+\delta$, respectively, in the medium, with $\delta \ll 1$. Then, the image point A' is the intersection of the two lines $\overline{PP'}$ and $\overline{QQ'}$, which are the refracted rays in the atmosphere (or a medium with lower index, n_a).

The equations of the two lines can be determined by applying the law of refraction at the impact points P and Q at the interface, respectively. At P,

$$\sin\theta' = n\sin\theta, \tag{A1}$$

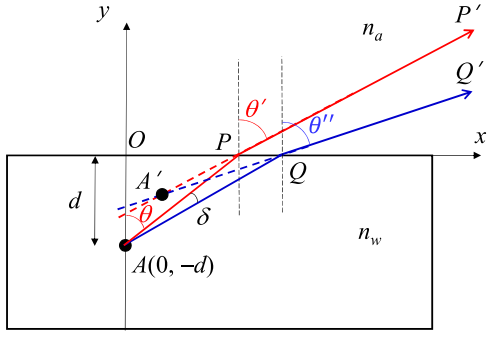

Fig. 6. Schematic diagram showing two rays emanating from a point source A, making oblique incidences at medium-atmosphere interface.

where $n = n_w/n_a$ is the relative refractive index, which is considered to be larger than 1. With the coordinates of the point $P(0,\, d\tan\theta)$, the equation of the line $\overline{PP'}$ is determined as

$$y = f(\theta)(x - d\tan\theta), \tag{A2}$$

where the slope $f(\theta)$ can be obtained from Eq. (A1) as

$$f(\theta) = \tan\left(\frac{\pi}{2} - \theta'\right) = \frac{\cos\theta'}{\sin\theta'} = \frac{\sqrt{1 - n^2\sin^2\theta}}{n\sin\theta} = \sqrt{\frac{1}{(n\sin\theta)^2} - 1}. \tag{A3}$$

For the line $\overline{QQ'}$, the equation is obtained similarly as

$$y = f(\theta + \delta)[x - d\tan(\theta + \delta)]. \tag{A4}$$

Eliminating x from Eqs. (A2) and (A4), we obtain

$$\frac{y}{f(\theta)} - \frac{y}{f(\theta + \delta)} = d[\tan\theta - \tan(\theta + \delta)], \tag{A5}$$

from which the y-coordinate of the intersection results as

$$y = -d\frac{f(\theta)f(\theta + \delta)}{f(\theta + \delta) - f(\theta)}[\tan(\theta + \delta) - \tan\theta]. \tag{A6}$$

For $\delta \ll 1$, one can approximate $f(\theta)f(\theta + \delta) \approx [f(\theta)]^2$. Furthermore, by expanding $f(\theta + \delta)$ and $\tan(\theta + \delta)$ in the Taylor series around θ, keeping the linear terms in d only, Eq. (1) is verified as

$$y = d[f(\theta)]^2\frac{\sec^2\theta}{\frac{df}{d\theta}} = -n^3 d\left(\frac{1}{n^2\sin^2\theta} - 1\right)^{\frac{3}{2}}\tan^3\theta = -\frac{d}{n}[1 - (n^2 - 1)\tan^2\theta]^{3/2}. \tag{A7}$$

The limiting case of $\theta \to 0$ clearly results in $y \to -d/n$, which is the apparent depth predicted by the Gaussian optics. However, when the angle of incidence increases, the apparent depth is reduced, approaching the interface until the critical angle ($\theta_c = \sin^{-1}n^{-1}$) is reached.

The x-coordinate of the intersection can also be determined by inserting Eq. (A7) into Eq. (A2), verifying Eq. (2):

$$x = d(n^2 - 1)\tan^3\theta \quad (0 < \theta < \theta_c). \tag{A8}$$

This explains the fact that the image gets closer to the viewer as the angle of incidence increases up to the critical angle θ_c. One can easily see from Eqs. (A7) and (A8) that the shift of the image point from the paraxial case is more significant for a material with a larger refractive index.

APPENDIX B: FRINGES FROM A WEDGED PLATE

Here, we consider the effects of a wedge angle between the two interface planes of a PPP. A tilt angle of α is assumed for the bottom plane of the PPP, as depicted in Fig. 7. This is a generalization of the geometry in Fig. 1, where perfect parallelism is assumed. We recalculated the OPD in Eq. (8) based on this new geometry.

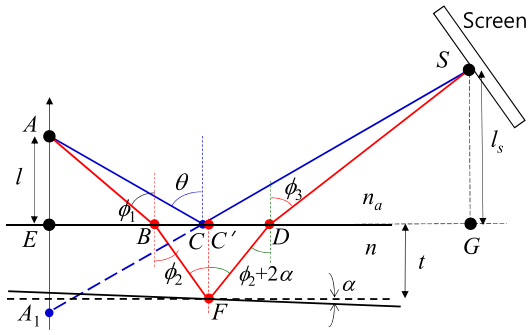

Fig. 7. This diagram is a slight modification of Fig. 1: Tilt angle α is assumed for the bottom plane.

While the optical path length of the first ray does not change [Eq. (3)], that of the second ray is altered due to the tilt of the bottom plane. In the figure, ϕ_1 is the angle of incidence at the top plane, and ϕ_2 is the angle of refraction related to ϕ_1 by the law of refraction:

$$\sin\phi_1 = n_r\sin\phi_2. \tag{B1}$$

We note that $\angle DFC' = \angle BFC' + 2\alpha = \phi_2 + 2\alpha$ because $\overline{C'F}$ is normal to the top plane. The emerging angle ϕ_3 is determined by the law of refraction applied at point D,

$$\sin\phi_3 = n_r\sin(\phi_2 + 2\alpha). \tag{B2}$$

The angles for the second ray can be determined by the relation,

$$\overline{EG} = \overline{EB} + \overline{BC'} + \overline{C'D} + \overline{DG}. \tag{B3}$$

As $\overline{EG} = r\sin\theta$, $\overline{EB} = l\tan\phi_1$, $\overline{DG} = l_s\tan\phi_3$, $\overline{BC'} = t\tan\phi_2$, $\overline{C'D} = t\tan(\phi_2 + 2\alpha)$, and $l + l_s = r\cos\theta$, Eq. (B3) can be written as

$$r\sin\theta = l\tan\phi_1 + l_s\tan\phi_3 + t[\tan\phi_2 + \tan(\phi_2 + 2\alpha)]. \tag{B4}$$

If we define the ratio $l/(l + l_s) \equiv \beta$, Eq. (B4) becomes

$$\sin\theta = \beta\cos\theta\tan\phi_1 + (1 - \beta)\cos\theta\tan\phi_3 + \frac{t}{r}[\tan\phi_2 + \tan(\phi_2 + 2\alpha)]. \tag{B5}$$

With the given parameters α, β, and t/r, Eqs. (B1), (B2), and (B4) can be solved to obtain the angles ϕ_1, ϕ_2, and ϕ_3 as functions of θ.

Then, the optical path length of the second ray can be calculated as

$$L_2 = n_a(\overline{AB} + \overline{DS}) + n(\overline{BF} + \overline{FD}) = n_a\left(\frac{l}{\cos\phi_1} + \frac{l_s}{\cos\phi_3}\right) + nt\left(\frac{1}{\cos\phi_2} + \frac{1}{\cos(\phi_2 + 2\alpha)}\right), \tag{B6}$$

and the phase difference is finally obtained:

$$\Phi(\theta) = \frac{2\pi n_a r}{\lambda}\left[\cos\theta\left(\frac{\beta}{\cos\phi_1} + \frac{1-\beta}{\cos\phi_3}\right) - 1 + \frac{n_r t}{r}\left(\frac{1}{\cos\phi_2} + \frac{1}{\cos(\phi_2 + 2\alpha)}\right)\right]. \quad \textbf{(B7)}$$

When $\beta = 0$, $\phi_1 = \phi_3$ by Eqs. (B1) and (B2). In this case, one can easily verify that this result is identical to Eq. (8), which is the phase difference for an ideal PPP.

Funding. National Research Foundation of Korea (2016R1D1A3B01006903).

Acknowledgment. This work was made possible in part by the Technology Research Initiative Fund Optics/Imaging Program at the University of Arizona. We thank D. W. Kim for verifying the polarization state of the light sources used in our experiments.

Disclosures. The authors declare no conflicts of interest.

REFERENCES

1. A. A. Michelson and E. W. Morley, "On the relative motion of the earth and the luminiferous ether," Am. J. Sci. **34**, 333–345 (1887).
2. B. P. Abbott, LIGO Scientific Collaboration, and VIRGO Collaboration, "Observation of gravitational waves from a binary black hole merger," Phys. Rev. Lett. **116**, 061102 (2016).
3. J. C. Wyant, "Use of an AC heterodyne lateral shear interferometer with real-time wavefront correction systems," Appl. Opt. **14**, 2622–2626 (1975).
4. J. B. Houston, Jr., C. J. Buccini, and P. K. O'Neill, "A laser unequal path interferometer for the optical shop," Appl. Opt. **6**, 1237–1242 (1967).
5. A. J. Werner, "Methods in high precision refractometry of optical glasses," Appl. Opt. **7**, 837–844 (1968).
6. M. S. Shummate, "Interferometric measurement of large index of refraction," Appl. Opt. **5**, 327–331 (1966).
7. S. D. Nicola, P. Ferraro, A. Finizio, and P. D. Natale, "A Mach–Zehnder interferometric system for measuring the refractive indices of uniaxial crystals," Opt. Commun. **202**, 9–15 (2002).
8. J. Chu and S.-W. Kim, "Absolute distance measurement by lateral shearing interferometry of point-diffracted spherical waves," Opt. Express **14**, 5961–5967 (2006).
9. F. L. Pedrotti, L. M. Pedrotti, and L. S. Pedrotti, *Introduction to Optics*, 3rd ed. (Pearson Education, 2014).
10. https://refractiveindex.info/.
11. C. Lee, H. Choi, J. Kim, M. Cha, and J. Jin, "Wavelength measurement by Fourier analysis of interference fringes through a plane parallel plate," Appl. Opt. **56**, 9638–9643 (2017).
12. G. J. Edwards and M. Lawrence, "A temperature-dependent dispersion equation for congruently grown lithium niobate," Opt. Quantum Electron. **16**, 373–375 (1984).